Frequency-Voltage-var Function for Active Front-end VFD on Oil and Gas Platforms with Offshore Wind Generation

Kassiane de S. Medeiros[1], João Marcus S. Callegari[1], Lorrana F. da Rocha[2], Danilo I. Brandao[1]

[1]Universidade Federal de Minas Gerais, Graduate Program in Electrical Engineering, Belo Horizonte, MG, Brazil.
[2]Norwegian University of Science and Technology, Department of Electric Energy, Trondheim, Norway.

e-mail: kassiane@ufmg.br, jmscallegari@ufmg.br, lorrana.faria@ntnu.no, dibrandao@ufmg.br.

ABSTRACT Renewable energy resources emerge as a sustainable alternative to augmenting the energy supply of floating production storage and offloading (FPSO) platforms. However, the increased generation at FPSO based on converter-interfaced energy decreases the system-equivalent inertia constant, which becomes more susceptible to frequency deviations. This paper proposes and evaluates the combined frequency-voltage-var control performance to mitigate frequency variation in a typical FPSO unit with penetration of floating wind energy generation. The control functions are communication-free and embedded in the active front-end variable frequency drives (AFE-VFDs), which are installed on the FPSO and have the primary function of controlling the speed of water injection pumps. The FPSO electrical power system model is developed in MATLAB/Simulink®. Comparative results obtained from the AFE-VFD equipped with volt-var, freq-var, and combined freq-volt-var functions are shown to highlight the proposed solution merits. The results have shown a conflicting behavior with the frequency and voltage deviation improvement associated with absorption and injection of reactive power, respectively. Accordingly, the frequency-volt-var prioritizes frequency deviations during heavy transient events and voltage deviations during regular operation.

KEYWORDS Control embedded in AFE-VFDs, Frequency support, Isolated power systems, Oil and gas production platforms, Offshore wind energy generation.

I. INTRODUCTION

Floating platforms are offshore structures for oil and gas (O&G) production with an anchoring system developed for deep-water exploration. The engineering challenges in deep waters (300–1500 m) and ultra-deep waters (beyond 1500 m) render using fixed offshore platforms impractical. The floating production storage and offloading (FPSO) is a floating platform that can, in most cases, produce, store, and transfer oil to a tanker cargo ship. According to [1], the FPSOs represent a compact and reliable alternative for the rapid decline in the discovery rate of large oil fields.

The FPSO power generation consists primarily of synchronous generators (SGs) driven by gas turbines, which feed loads through a medium-voltage (MV) bus. The electrical energy consumption can reach tens of megawatts due to specific functions, the complexity of the system, and environmental conditions [2]. Since the main energy generation on FPSOs is achieved through SGs powered by gas turbines, the platform operation is associated with high inertia and carbon emissions [3].

The sustainable expansion of FPSO power generation is highly desired to support production growth environmentally

friendly. Floating offshore wind power generation has proven to be a viable solution for such a challenge [4]. However, the FPSO is isolated from the conventional grid, which configures a weak power system and is susceptible to electrical disturbances. In this context, the inherent intermittency of wind-based generation can affect FPSO power quality issues concerning frequency and voltage. Also, the inclusion of wind-based energy causes an inertia constant (H) decrease when compared to increased generation by adding more SGs [5].

Several papers in the literature focus on frequency support for electrical systems connected to offshore wind farms. However, many of these publications concentrate on offshore wind farms connected to electrical grids onshore via high-voltage direct current (HVDC) transmission systems. Publications [6]–[11] use converter control techniques with the energy from the wind farm, and in some cases from extra sources of energy storage. The authors of [6] propose a frequency control through virtual inertia emulation. In [7] and [8], the authors employ reverse droop relations: active power related to voltage ($P - v$) and reactive power related to frequency ($Q - f$). The authors of [9] and [10] propose the

implementation of droop controls in grid-forming converters. Reference [9] uses conventional droop functions ($Q - v$ and $P - f$), while [10] employs reactive power-frequency ($Q - f$) droop. The authors of [11] apply $P - \omega_r$ and $P - f$ droop controls, where P, ω_r and f represent the wind turbine active power, rotor speed, and power system frequency, respectively.

On the other hand, the authors of [12]–[19] address frequency support for offshore electrical grids integrated with offshore wind farms. In [12], [13], and [17], control strategies with the energy from wind turbines are proposed for frequency regulation. While the authors of [13] apply inertia emulation for frequency control, the authors of [12] implement conventional voltage and frequency droop controls, $P - f$ and $Q - v$. The publications [14], [15] and [16] include an energy storage system (ESS) for frequency support, approaching sizing methodologies to determine the appropriate power and energy for the ESS. The authors of [18] explore frequency regulation using active power from ESSs and motors. However, solutions that require additional space and weight are challenging for offshore applications. The authors of [17] propose using $P - f$ droop control in conjunction with pitch control and deloading techniques. A coordinated control strategy is proposed in [19] by digitally implementing the volt-var ($Q-v$) function in active front-end variable frequency drives (AFE-VFDs). Herein, the reactive power is processed through the AFE-VFDs, as in [19], nonetheless for frequency support.

On FPSOs, the largest motors are usually equipped with diode front-end variable frequency drives (DFE-VFDs). The DFE-VFDs can improve efficiency, AC speed control, soft start, and limit motor transient short-circuit current contribution. The drawback of DFE-VFD installation is that it reduces the equivalent system inertia. The motors driven by DFE-VFDs stop contributing to inertia since they become electrically decoupled from the main busbar. The connection of a wind energy conversion system (WECS) to the FPSO also decreases the equivalent FPSO inertia since it increases the power generation with a null inertia contribution. In this context, an increase in voltage and frequency variations is expected, which may exceed the standard limits. In this circumstance, replacing DFE-VFDs with AFE-VFDs embedded with active and reactive power processing functions to regulate voltage and/or frequency is highly desirable. The frequency regulation positively affects the system equivalent inertia. Therefore, this paper proposes a decentralized control solution implemented on AFE-VFDs to support frequency and avoid footprint allocation for new equipment on the FPSO.

Thus, the contribution of this paper is to propose and evaluate the performance of the combined function frequency-voltage-var (freq-volt-var). The freq-volt-var function is digitally implemented at AFE-VFDs and processes reactive power to frequency and voltage support. The precedence is for frequency support, supposing frequency deviations above an established threshold. In case frequency deviations do not exceed the established threshold, voltage support is enabled. This paper is an extended version of [20], in which an analysis of the X/R characteristics of the FPSO cables and their relationship with the use of reactive power processing to support frequency and voltage is added. Furthermore, a procedure for tuning the notable points of the freq-volt-var curve is shown as a novelty. The FPSO electrical power system is simulated in MATLAB/Simulink®. The proposed strategy is compared with two other related works in literature: volt-var and freq-var [21]. The comparisons are made to highlight the superiority of the proposed method applied to the FPSO power system. The figures of merit used to evaluate the control performance during steady-state and transient events are voltage and frequency variations, frequency nadir, rate of change of frequency (RoCoF), and system inertia constant.

This paper is structured as follows. Section II presents the FPSO electrical power system and the cable characteristics related to the use of reactive power processing to frequency support. Section III shows the functions implemented at AFE-VFDs: volt-var, freq-var, and freq-volt-var. In addition, it describes the tuning procedure for the proposed freq-volt-var. Comparative simulation results are shown in Section IV. Finally, Section V concludes this paper.

II. FPSO UNIT WITH FLOATING OFFSHORE WIND

Fig. 1 shows a 50 MW wind farm integrated into the electrical power system of a typical Brazilian FPSO from Mero Oil Field through a 12 km umbilical cable. Five WECS, each composed of a 10 MW wind turbine, a permanent magnet synchronous generator (PSMG), a back-to-back converter, and an LCL output filter, are employed herein. The back-to-back converter is controlled in grid-following mode to minimize the umbilical cable transmission losses. Three 36.25 MVA SGs driven by 29 MW gas turbines compose the FPSO main power generation. Each SG has 3175 kgm^2 of inertia moment and 1800 rpm of rated speed, contributing then with 1.56 s of inertia constant, as similarly found in [14]. The SGs are equipped with frequency and voltage slow dynamic secondary control to achieve steady-state regulation at 60 Hz and 11 kV, respectively. Conforming to Fig. 1, an MV load, low-voltage (LV) loads fed by step-down transformers, and MV motors are connected to two MV busbars, referred to as Topsides and Vessel. The motors, such as compressors and water injection pumps, store kinetic energy in their rotors. When directly connected to the FPSO busbar, they contribute to frequency stability and enhance the FPSO equivalent inertia. The circuit breakers between the Topsides and Vessel buses are closed, as shown in Fig. 1. This arrangement configures a radial system, which simplifies the protection functions required for the safe operation of the FPSO.

The case study of this paper contains two 16 MVA AFE-VFDs driving two water injection pumps, as represented in Fig. 1. According to [22], in the context of power electronics-based technologies development, the connection
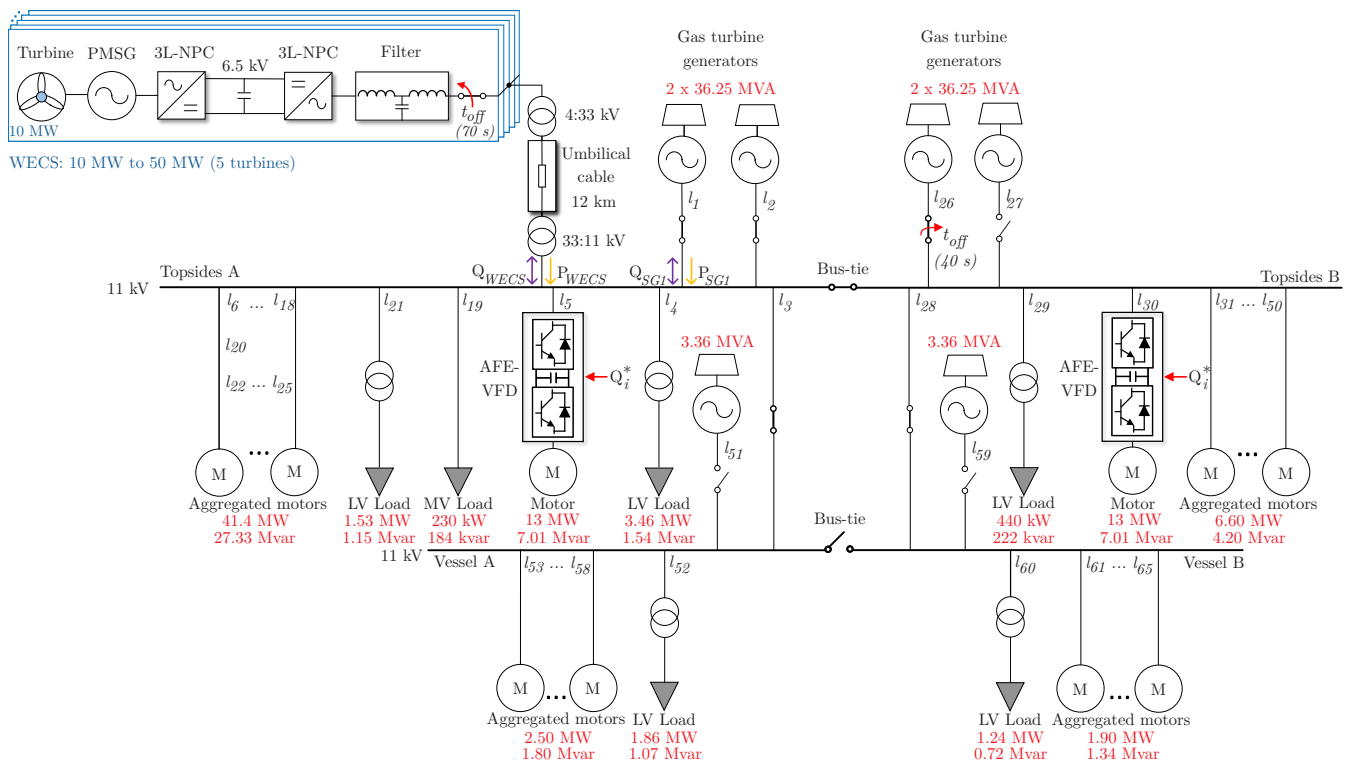
FIGURE 1. Simulated electrical power system of a typical Brazilian FPSO from Mero Oil Field with two AFE-VFDs.

of crucial equipment through AFE-VFDs has become a widely accepted solution to mitigate the drawbacks of the all-electric FPSO. Among the commercially available topologies, the cascaded H-bridge converter with DFE rectifier is a cost-effective solution widely used [23]. The cascaded H-bridge converter has speed and torque control of the onboard motors with minimum maintenance requirements. Nonetheless, the passive rectifier stage produces high levels of harmonic distortion without any inertia contribution, which is undesirable in offshore systems [24]. This issue is overcome by employing the AFE-VFD. In AFE-VFDs, the input waveform is less harmonic polluted, and the drive has a feature 4-quadrant speed-torque operation (i.e., allowing energy regeneration from the motor to the main feeder). Furthermore, it is possible to enable grid-side unity power factor operation [25]. Detailed parameters for each piece of equipment used in the FPSO model can be found in [26]. Notably, the proposed control strategy is evaluated through simulation results, considering a real-case test bench where the main operating results of the FPSO were validated against real tests conducted on a Brazilian offshore platform.

A. REACTIVE POWER PROCESSING FOR FREQUENCY AND VOLTAGE SUPPORT

The literature widely identifies the coupling between active power and frequency $(P - f)$ and reactive power and voltage $(Q - V)$ [21] for electrical power systems with line impedances that feature an X/R ratio greater than one (induc-

tive grid). This inductive characteristic of line impedance is found predominantly in medium and high-voltage systems. Conversely, $P - V$ and $Q - f$ couplings occur in electrical power systems with resistive impedances, where the X/R ratio is less than one, typical of low voltage grids [27]. The droop controls are considered conventional when the relationships $P - f$ and $Q - V$ are used for frequency and voltage regulation, respectively.

As shown in the Appendix, the FPSO system, the case of study of this paper, has approximately 32% of lines with inductive characteristics, with an average of $X/R = 1.93$, and 68% of lines with resistive characteristics with an average of $X/R = 0.30$. Since the FPSO system comprises cables with varying X/R ratios, a coupling between $P - V - f$ and $Q - V - f$ is expected. Based on this premise, this paper adopts frequency-voltage-var control, which operates on $Q - f$ and $Q - V$ couplings. It is essential to highlight that the inductive characteristic ($X/R = 2.11$ and $X/R = 2.08$) of the lines where the AFE-VFDs are connected (i.e., l_5 e l_{30}) provides a more significant coupling of reactive power to voltage. The Appendix shows the FPSO power lines, insulated for 15 kV.

III. VOLTAGE CONTROL AND FREQUENCY SUPPORT USING REACTIVE POWER THROUGH THE AFE-VFDs

Due to the power electronics embedded in the AFE rectifier cells, the reactive power exchanged with the FPSO can be explored to improve voltage and frequency fluctuations. Reactive power configures a degree of freedom in AFE-
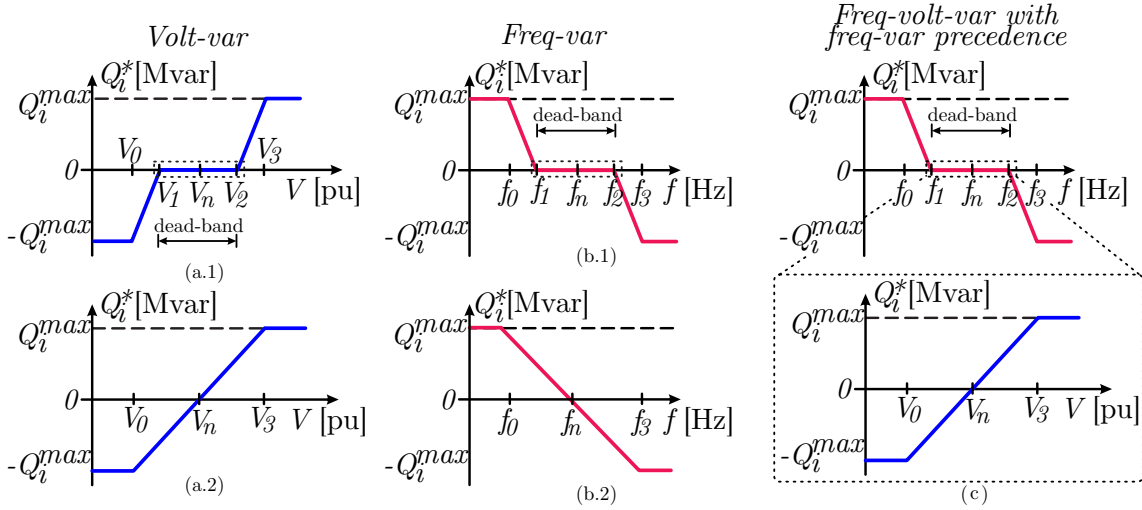
FIGURE 2. Communication-free functions digitally implemented on the i-th AFE-VFD: (a.1) volt-var with dead-band; (a.2) volt-var without dead-band; (b.1) freq-var with dead-band; (b.2) freq-var without dead-band; and (c) freq-volt-var with freq-var precedence.

VFDs, in contrast with active power, which depends on the motor shaft load. The dq-reference frame control loops implemented at the AFE-VFD are described in [26]. Reactive power references of the grid-side converter are calculated by the autonomous control functions described below and are provided for two AFE-VFDs set on water injection pumps.

Figs. 2 (a)-(c) show the communication-free functions: the volt-var, the freq-var, and the proposed combined freq-volt-var, all locally implemented at AFE-VFDs. According to Fig. 2, the curves are defined by intervals in which the AFE-VFDs give instructions regarding reactive power injection or absorption (Q). The dead-band defines the interval at which the AFE-VFDs do not exchange reactive power with the power system. Q_i^* is real-time reactive power injected or absorbed computed based on the i-th AFE-VFD idle power availability, i.e., $\sqrt{(S_{n,i}^{VFD})^2 - (P_i^{VFD})^2}$, in which $S_{n,i}^{VFD}$ and P_i^{VFD} are the rated apparent power and actual active power processed by the i-th AFE-VFD, respectively. All idle reactive power capacity available in AFE-VFDs is exploited within the limits from $-Q_i^{max}$ to Q_i^{max}.

Fig. 2 (a.1) shows the volt-var function with the dead-band defined within v_1 and v_2. For FPSO voltage higher than v_3 or less than v_0, the AFE-VFD processes Q_i^{max} (inductive) and $-Q_i^{max}$ (capacitive), respectively. The volt-var curve is centered on the FPSO-rated voltage, i.e., $v_n = 1$ pu. Similarly, for the freq-var function, the dead-band limits are defined within f_1 and f_2, as shown in Fig. 2 (b.1). For FPSO frequency higher than f_3 or less than f_0, the AFE-VFD processes $-Q_i^{max}$ (capacitive) and Q_i^{max} (inductive), respectively. The midpoint relative to the frequency axis is set to $f_n = 60$ Hz. Figs. 2 (a.2) and (b.2) show the volt-var and freq-var curves without dead-band, while Fig. 2 (c) shows the proposed freq-volt-var curve with frequency support precedence. The points mentioned above, v_0, v_1, v_2, v_3, f_0, f_1, f_2, f_3, which delimit the different voltage and frequency control curves regions, are referred on this study as notable points.

A. VOLT-VAR FUNCTION

The volt-var function is a well-established piece-wise linear voltage curve as a function of reactive power [21]. This curve can be implemented with or without dead-band, as shown in Figs. 2 (a.1) and (a.2), respectively. The volt-var function with dead-band is described by (1), while the volt-var function without dead-band is described by (2).

$$Q_i^* = \begin{cases} -Q_i^{max}, \text{ if } v < v_0 \\ \frac{Q_i^{max}(v - v_1)}{(v_1 - v_0)}, \text{ if } v_0 \leq v < v_1 \\ 0, \text{ if } v_1 \leq v < v_2 \\ \frac{Q_i^{max}(v - v_2)}{(v_3 - v_2)}, \text{ if } v_2 \leq v < v_3 \\ Q_i^{max}, \text{ se } v \geq v_3 \end{cases} \quad (1)$$

$$Q_i^* = \begin{cases} -Q_i^{max}, \text{ if } v < v_0 \\ \frac{Q_i^{max}(2v - v_0 - v_3)}{(v_3 - v_0)}, \text{ if } v_0 \leq v < v_3 \\ Q_i^{max}, \text{ if } v \geq v_3 \end{cases} \quad (2)$$

where Q_i^* is the reactive power reference applied to the AFE-VFD control loop [26] and v is the root-mean-square (RMS) voltage measured at the AFE-VFD output terminals.

B. FREQ-VAR FUNCTION

The freq-var function is defined in Figs. 2 (b.1) and (b.2) with and without dead-band, respectively. It is a piece-wise linear frequency curve as a function of reactive power. The curves with and without dead-band are defined in (3) and (4), respectively.

$$Q_i^* = \begin{cases} Q_i^{max}, & \text{if } f < f_0 \\ \frac{Q_i^{max}(f-f_1)}{(f_0-f_1)}, & \text{if } f_0 \leq f < f_1 \\ 0, & \text{if } f_1 \leq f < f_2 \\ \frac{Q_i^{max}(f-f_2)}{(f_2-f_3)}, & \text{if } f_2 \leq f < f_3 \\ -Q_i^{max}, & \text{if } f \geq f_3 \end{cases} \quad (3)$$

$$Q_i^* = \begin{cases} Q_i^{max}, & \text{if } f < f_0 \\ \frac{Q_i^{max}(2f-f_0-f_3)}{(f_0-f_3)}, & \text{if } f_0 \leq f < f_3 \\ -Q_i^{max}, & \text{if } f \geq f_3 \end{cases} \quad (4)$$

where f is the frequency estimated by a phase-locked loop (PLL) algorithm from the voltage measurement at the AFE-VFD output terminals.

C. PROPOSED COMBINED FREQUENCY-VOLTAGE-VAR FUNCTION

The combined freq-volt-var function is shown in Fig. 2 (c). The proposed curve is composed of the volt-var function without a dead-band and the freq-var function with a dead-band. The freq-var function precedes the volt-var function, i.e., frequency deviations greater than f_2 or less than f_1 enable the volt-var curve, as described in (5) and (6).

$$Q_i^* = \begin{cases} Q_i^{max}, & \text{if } f < f_0 \\ \frac{Q_i^{max}(f-f_1)}{(f_0-f_1)}, & \text{if } f_0 \leq f < f_1 \\ Q_{i\,volt-var}^*, (Eq.\ 6), & \text{if } f_1 \leq f < f_2 \\ \frac{Q_i^{max}(f-f_2)}{(f_2-f_3)}, & \text{if } f_2 \leq f < f_3 \\ -Q_i^{max}, & \text{if } f \geq f_3 \end{cases} \quad (5)$$

$$Q_{i\,volt-var}^* = \begin{cases} -Q_i^{max}, & \text{if } v < v_0 \\ \frac{Q_i^{max}(2v-v_0-v_3)}{(v_3-v_0)}, & \text{if } v_0 \leq v < v_3 \\ Q_i^{max}, & \text{if } v \geq v_3 \end{cases} \quad (6)$$

The proposed freq-volt-var strategy differs from others in the literature, since the volt-var function is triggered under steady-state conditions, while freq-var function is triggered under transient events. The proposed control is locally managed based on the AFE-VFDs-driven load demand, therefore active power processing is not considered in the proposed control.

D. PROPOSED FREQ-VOLT-VAR CURVE TUNING PROCEDURE

The main goal of the proposed freq-volt-var function is to regulate the frequency. The freq-volt-var curve comprises a dead zone, limited for the notable points f_1 and f_2, and straight lines with a slope depending on the saturation points, f_0 and f_3. Saturation points are the frequency values in which the reactive power reaches the limit imposed by the available amount of AFE-VFD power. For the freq-var and volt-var, the dead-band is the curve region with no reactive power sharing. Nevertheless, for the freq-volt-var, the dead-band is also the frequency range in which reactive power sharing stops processing for frequency regulation and starts
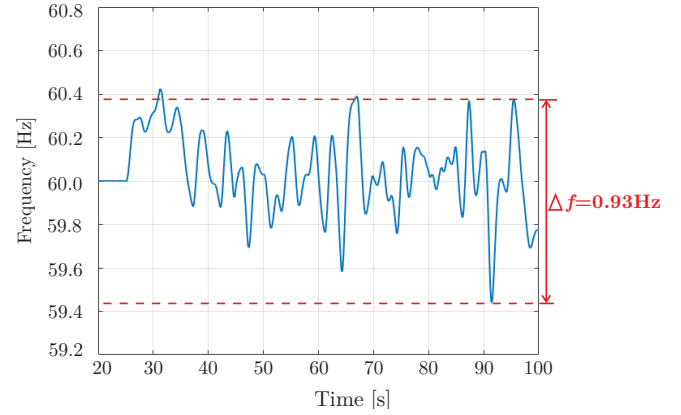

FIGURE 3. Frequency behavior in the absence of transients.

TABLE 1. Voltage and frequency tolerances according to IEC 61892 standard [28].

Profile	Steady-state	Transient
Frequency	$\pm 5.0\%.f_n$	$\pm 10\%.f_n$
Voltage	$\pm 2.5\%.v_n$	$+20\%.v_n$, $-15\%.v_n$

processing for voltage regulation. Whereas the freq-volt-var strategy is designed for frequency support during transient events and voltage support during the conditions considered by this paper steady-state.

1) Dead-band definition

Fig. 3 shows the FPSO frequency behavior under steady-state conditions, i.e., without transient events. The frequency deviations shown in Fig. 3 are caused by the intermittent WECS generation interconnected to the FPSO, leading to a maximum frequency oscillation of approximately 0.93 Hz. Based on this empirical value, the dead-band is set at 1 Hz (notable points: f_1 = 59.5 Hz, f_2 = 60.5 Hz) to ensure that the freq-var activates only during transient events.

2) Saturation points definition

The standard IEC 61892 [28] is used as a reference for the tuning procedure for points associated with Q_i^{max} and $-Q_i^{max}$, i.e., the notable points f_0 and f_3 for activated frequency support, and v_0 and v_3 for activated voltage regulation. Table 1 shows the acceptable deviation for frequency and voltage, during steady-state conditions and transient events, according to IEC 61892 standard.

From the tolerances defined by the IEC 61892 standard, curve slope values are tested as shown in Figs. 4 and 5. The notable points f_0 and f_3 ranges from ± 6 Hz (IEC 61892 reference, $\pm 10\%$ of f_n) to ± 1 Hz, as shown in Fig. 4. Similarly, the notable points v_0 and v_3 ranges from 1.2 pu (IEC 61892 reference, $\pm 20\%$ of v_n) to 1.05 pu, as shown in Fig. 5. The frequency intervals between f_0 - f_1, and between f_2 - f_3 in the freq-volt-var are designated as
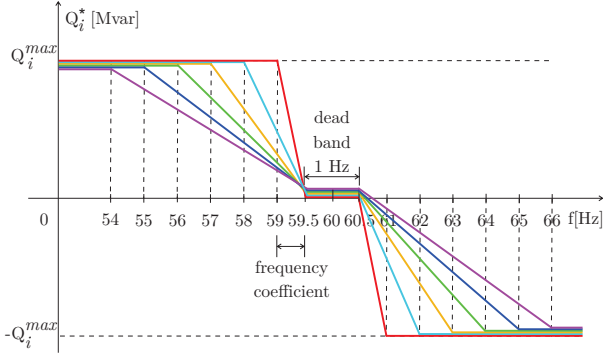
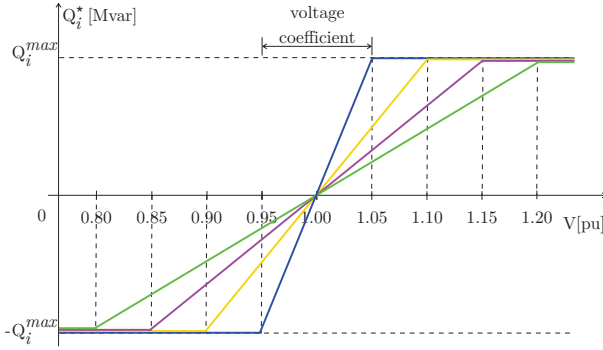**FIGURE 4. Freq-volt-var curves with 1 Hz dead-band and notable points tested.**

FIGURE 5. Volt-var curve actived during freq-volt-var dead-band with notable points tested.

FIGURE 6. Frequency RMSE.

FIGURE 7. Voltage RMSE.

frequency coefficients, while the voltage interval, from f_0 to f_3 is referred to as the voltage coefficient. Therefore, six frequency coefficients, from 0.5 Hz to 5.5 Hz, and four coefficients for voltage, from 0.1 pu to 0.4 pu, are tested.

The root mean square error (RMSE) quantifies the performance of freq-volt-var under the tested frequency and voltage coefficients.

$$RMSE = \sqrt{\frac{1}{n}\sum_{i=1}^{n}(y_i - p_i)^2} \qquad (7)$$

where n represents the number of analyzed results, y_i is the measured values, and p_i is the nominal references.

Fig. 6 shows the RMSE for frequency results correlate to frequency coefficients. Fig. 7 shows the evolution of the RMSE for voltage results correlated to the voltage coefficients. According to Fig. 6, the increase in the frequency RMSE error follows the increase in the frequency coefficient. While the variation in the voltage coefficient does not significantly affect the frequency RMSE error. From these results, the frequency coefficient used in the freq-volt-var implementation is 0.5 Hz (from dead-band), which corresponds to f_0 = 59 Hz and f_3 = 61 Hz. Following the RMSE parameter, these values present the best performance among the analyzed cases, without exceeding the IEC 61892 requirements.
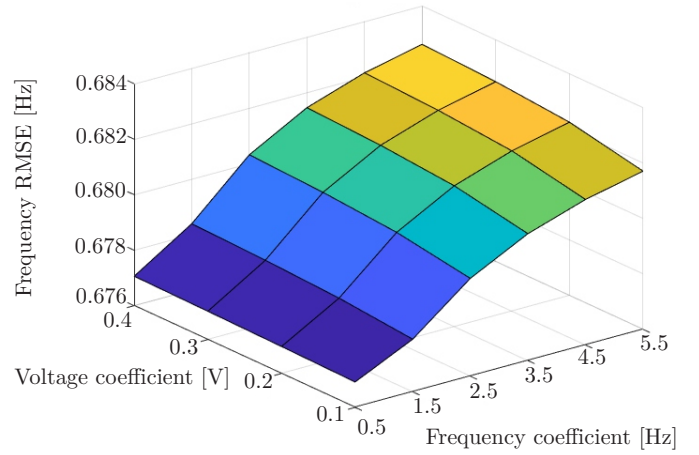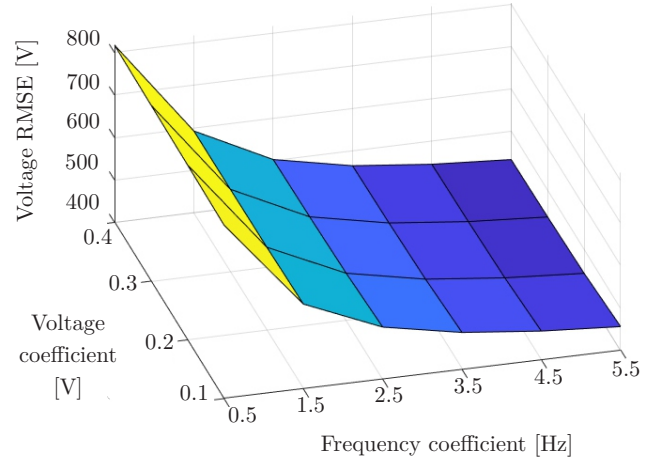
Analysis of the results in Fig. 7 reveals that increasing the voltage coefficient leads to the largest RMSE error among the cases analyzed. Therefore, the smallest tested voltage coefficient, 0.10 pu, is applied, corresponding to v_0 = 0.95 pu and v_3 = 1.05 pu. Increasing the frequency coefficient reduces the voltage RMSE error. However, the frequency coefficient is set up first, in order to prioritize the frequency support performance. The notable points selected for the volt-var function show the best performance according to the RMSE error and do not exceed the IEC 61892 requirements. Table 2 shows the notable points for the tested functions. As shown in Fig. 2, the combined freq-volt-var with freq-var precedence comprises the freq-var with dead-band and volt-var without dead-band.

E. EVALUATED FIGURES OF MERIT
Power quality issues may increase on the FPSO due to the intermittent generation of wind power. Additionally, the reduction in system inertia caused by the use of AFE-VFDs without inertia control also contributes to an increase in

TABLE 2. **Notable Points.**

	freq-var				volt-var		
	with dead-band		without dead-band		with dead-band		without dead-band
f_0	59.0	f_0	59.0	V_0	0.950	V_0	0.95
f_1	59.5			V_1	0.975		
f_n	60.0	f_n	60.0	V_n	1.000	V_n	1.00
f_2	60.5			V_2	1.025		
f_3	61.0	f_3	61.0	V_3	1.050	V_3	1.05

frequency variation. Herein, the power system quality issues are quantified by the following figures of merit:

1) Voltage variation: $\Delta V = V_{max} - V_{min}$.
2) Frequency variation: $\Delta f = f_{max} - f_{min}$.
3) Frequency nadir: f_{nadir}.
4) RoCoF [29]: $RoCoF_{0.5s} = (f_{0.5} - f_0)/0.5$.
5) Inertia constant [30]: $H = -\Delta P/(2 \cdot RoCoF_{0.5s})$.

During the steady-state condition, the minimum and maximum values of voltage and frequency are evaluated within two predetermined time windows. The figures of merit f_{nadir}, RoCoF, and H are calculated to evaluate frequency deviations associated with transient events. f_{nadir} is defined as the minimum frequency reached after the disturbance, and the RoCoF is the time derivative of the power system frequency (df/dt). The RoCoF is typically estimated by using two frequency measurements within a short period (i.e., 0.5 seconds) immediately following a sudden disturbance [29]. Until that time, which is before the response of most turbine governors to the frequency deviation, the system response depends primarily on the size of the contingency and the system inertial response. Lastly, H is estimated by the relation between the amount of generation loss and the system RoCoF immediately after the transient event [30]. These measurements are discussed by comparing the communication-free control functions implemented at the AFE-VFDs: volt-var, freq-var, and combined freq-volt-var.

IV. SIMULATION RESULTS

Section IV.A compares AFE-VFDs set up to unity power factor (PF = 1); volt-var with dead-band; and volt-var without dead-band. Section IV.B also addressed three scenarios: AFE-VFDs with PF = 1, freq-var with dead-band, and freq-var without dead-band. The better performances related to the presence or absence of dead-band at the curve are applied to compose combined freq-volt-var control. Section IV.C compares the results of volt-var, freq-var, and freq-volt-var implementing.

The figures of merit established at Section III. E are evaluated for two steady-state periods ($30 \leq t < 40$ s and $80 \leq t < 90$ s) and two transient events (at 40 s and 70 s). In addition to the three control settings, the numeric results for the FPSO without AFE-VFDs, i.e., the 13 MW motors are directly connected to the 11 kV busbar and operating with

PF = 1, are also presented. The simulated transient events are the sequence of generation loss following:

- at $t = 40$ s, an unscheduled interruption of one SG is performed ($N_{SG} = 3 \rightarrow 2$);
- at $t = 70$ s, an unscheduled shutdown of one wind turbine is simulated ($N_t = 5 \rightarrow 4$).

These transient events are computed for time windows: $40 \leq t < 44$ s and $70 \leq t < 74$ s.

A. COMPARISON BETWEEN PF = 1, VOLT-VAR CONTROL WITH DEAD-BAND, AND VOLT-VAR CONTROL WITHOUT DEAD-BAND

Fig. 8 shows a set of results composed of active and reactive powers at: (a) SG_1, (b) WECS and (c) AFE-VFDs; (d) voltage; and (e-g) frequency. Only SG_1 data are addressed due to the power system symmetry and the power-sharing derived from the droop-based control of the SGs. As can be seen in Fig. 8 (a) and (b), SGs complement the intermittent active power generated by the WECS, which leads to a natural oscillation in the FPSO frequency due to the governor slow dynamics - see Fig. 8 (e). As a result of the power coupling caused by the FPSO line impedances and the slow dynamics of the SG automatic voltage regulator (AVR), the main busbar voltage also oscillates with the WECS penetration -see Fig. 8 (d).

From Fig. 8 (d), immediately after 40 s, the FPSO voltage sag reaches 0.93 pu, considering the AFE-VFDs controlled for PF = 1. With volt-var set up with dead-band, this FPSO RMS voltage sag improves from 0.93 to 0.96 pu. While programmed with volt-var without dead-band, the improvement is to 0.97 pu. This difference is explained due to a higher positive slope of the volt-var curve with dead-band, in the intervals between v_0 - v_1, and v_2 - v_3 - see Fig. 2 (a.1), compared to the volt-var curve slope without dead-band, between v_0 - v_3 - see Fig. 2 (a.2). A higher positive slope is associated with a higher capacity for voltage regulation.

Moreover, during the 50 s to 68 s, steady-state improvement of FPSO voltage regulation is seen when the AFE-VFDs operate with the volt-var curve without dead-band ($\Delta V = 6.94$ x 10^{-3} V) compared to the case with dead-band ($\Delta V = 14.44$ x 10^{-3} V) - see the enlarged view of Fig. 8 (d). On the other hand, no improvement or deterioration is observed in the frequency variation with the presence or absence of the dead-band, during steady-state (i.e., Fig. 8 (c)) or transient (i.e., Figs. 8 (f)-(g)). Due to this lower voltage variation in steady-state, the volt-var without dead-band is adopted for the proposed combined freq-volt-var strategy.

B. COMPARISON PF = 1, FREQ-VAR CONTROL WITH DEAD-BAND, AND FREQ-VAR CONTROL WITHOUT DEAD-BAND

Figs. 8 (h)-(n) show steady-state and transient results for the scenario characterized by AFE-VFDs embedded into the
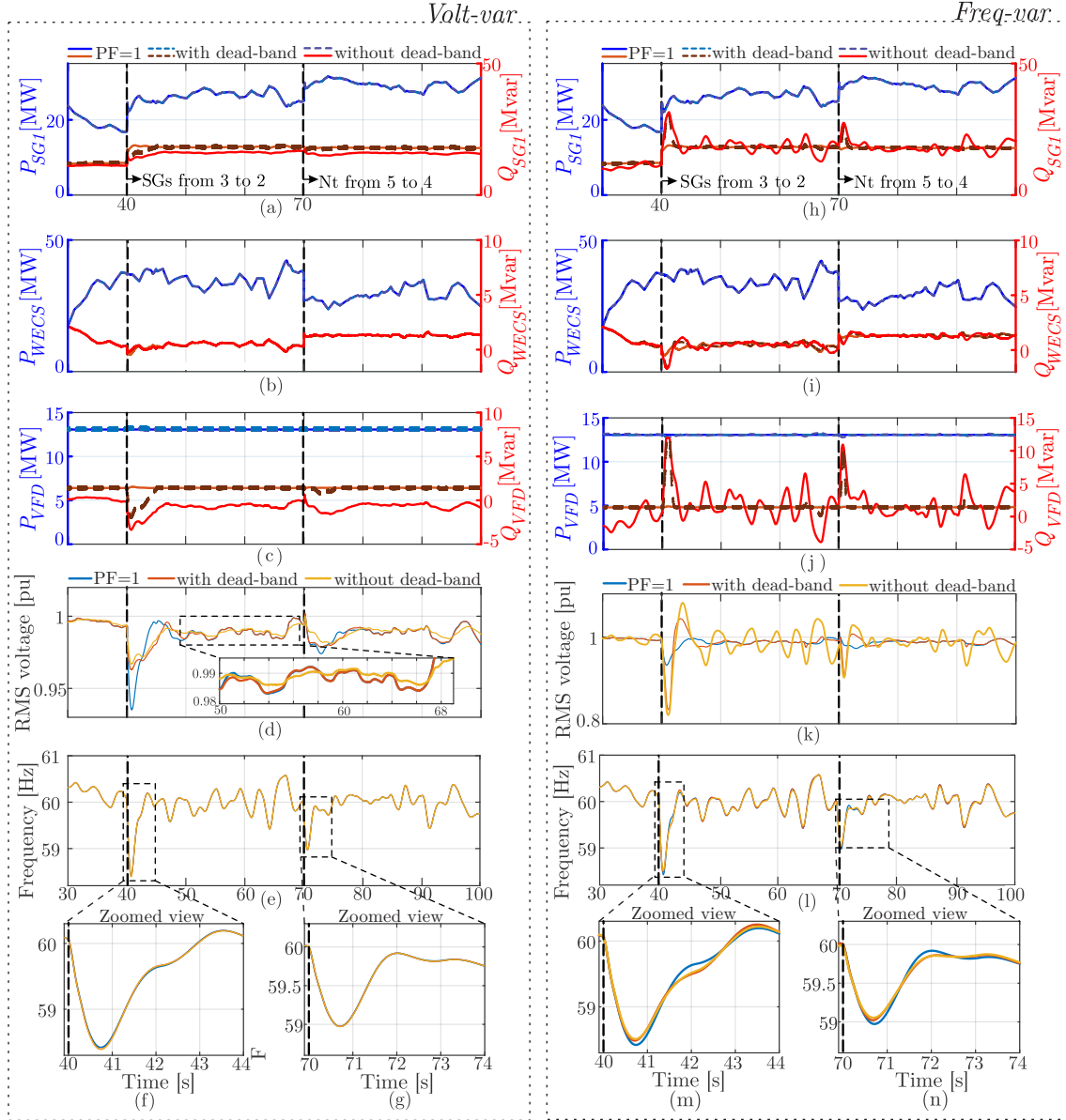
FIGURE 8. Simulated results considering AFE-VFD embedded with volt-var and freq-var, with and without dead-band: (a) active and reactive power at SG$_1$, (b) active and reactive power at WECS, (c) active and reactive power at AFE-VFD terminals, (d) Topsides busbar voltage, (e-g) FPSO frequency.

TABLE 3. Summary of the results sampled from Fig. 9.

| Function Control	Steady-state				Transient-state					
	$30 \leq t < 40s$		$80 \leq t < 90s$		$40 \leq t < 44s$			$70 \leq t < 74s$		
	$N_{SG} = 3, N_t = 5$		$N_{SG} = 2, N_t = 4$		$N_{SG} = 3 \rightarrow 2, N_t = 5$			$N_{SG} = 2, N_t = 5 \rightarrow 4$		
	ΔV	Δf	ΔV	Δf	f_{nadir}	$ROCOF_{0.5s}$	H	f_{nadir}	$ROCOF_{0.5s}$	H
	(pu)	(Hz)	(pu)	(Hz)	(Hz)	$(1/s^2)$	(s)	(Hz)	$(1/s^2)$	(s)
without AFE-VFDs	7.05×10^{-3}	0.52	5.59×10^{-3}	0.44	58.64	2.55	3.53	59.11	1.61	3.36
PF = 1	6.58×10^{-3}	0.54	4.82×10^{-3}	0.53	58.42	2.92	3.08	58.97	1.87	2.90
volt-var	4.51×10^{-3}	0.54	2.72×10^{-3}	0.53	58.39	2.98	3.02	58.97	1.87	2.91
freq-var	6.58×10^{-3}	0.54	6.59×10^{-3}	0.53	58.49	2.87	3.14	59.02	1.83	2.97
freq-volt-var	4.51×10^{-3}	0.54	2.27×10^{-3}	0.53	58.47	2.90	3.10	59.02	1.82	2.98
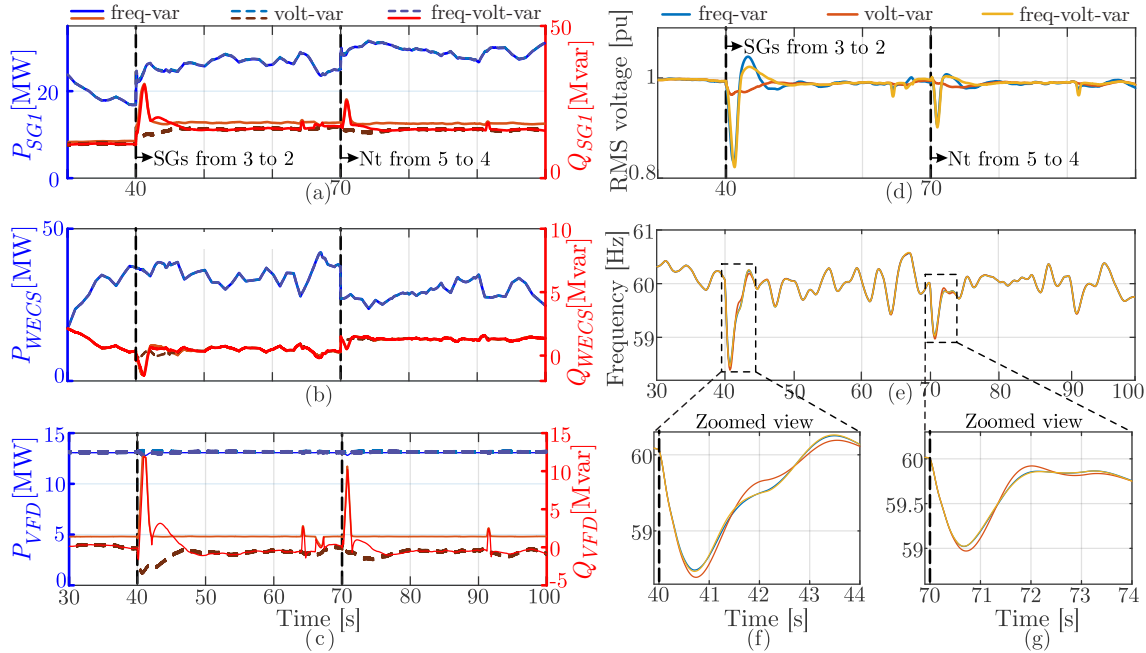
FIGURE 9. Simulated results considering AFE-VFD embedded with volt-var, freq-var, and freq-volt-var: (a) active and reactive power at SG_1, (b) active and reactive power at WECS, (c) active and reactive power at AFE-VFD terminals, (d) Topsides busbar voltage, (e-g) FPSO frequency.

FPSO operating with PF = 1 and equipped with the freq-var curves with and without dead-band. Figs. 8 (h)-(j) shows active and reactive powers at (h) SG_1, (i) WECS, and (j) AFE-VFDs. Notably, the reactive power profile of the AFE-VFD, when programmed with the freq-var functions, exhibits greater oscillations compared to the same device configured with the volt-var functions. With the volt-var function, the maximum Q_{VFD} injected is 3.35 Mvar in the transient event (after 40 s) and 1.47 Mvar in steady-state - see Fig. 8 (c). While with the freq-var function, the maximum Q_{VFD} absorbed is 11.97 Mvar in the transient event (after 40 s) and 6.55 Mvar in steady-state - see Fig. 8 (j).

The greater amount of reactive power processed by the AFE-VFD configured for frequency regulation affects the FPSO voltage. This voltage disturbance is associated with the coupling between voltage and reactive power due to the inductive portion of the FPSO power system upstream to the AFE-VFD connection, as shown in Table 4. The most considerable voltage oscillations are associated with the implementation of freq-var without dead-band. In such a scenario, the voltage variation reaches $\Delta V = 0.26$ pu in the transient event (after the SG shutdown at 40 s) and $\Delta V = 0.11$ pu in steady-state condition. The RMS voltage, considering the implementation of freq-var with dead-band, corresponds to the RMS voltage for PF = 1, except at the instants following the transient events. The voltage variation for freq-var control with dead-band implemented is $\Delta V = 0.03$ pu in the transient event (after the SG shutdown at 40 s) and $\Delta V = 0.01$ pu in steady-state.

The frequency behavior during the steady-state shows a negligible difference with PF = 1 or with the employment of the freq-var curves - see Fig. 8 (l). On the other hand, after the first transient event (t = 40 s), the frequency nadir shows a recovery from 58.42 Hz (PF = 1) to 58.49 Hz (freq-var with dead-band) and 58.51 Hz (freq-var without dead-band) - see Fig. 8 (m). After the second transient event (t = 70 s), the following metrics are computed: f_{nadir} = 58.97 Hz (PF = 1), f_{nadir} = 59.02 Hz (freq-var with dead-band), and f_{nadir} = 59.05 Hz (freq-var without dead-band) - see Fig. 8 (n). The frequency nadir results for freq-var with and without dead-band are similar. The reduced effect on FPSO voltage with the employment of freq-var with the dead-band defines the employment of this curve on the proposed combined freq-volt-var.

C. COMPARISON BETWEEN VOLT-VAR, FREQ-VAR, AND COMBINED FREQ-VOLT-VAR FUNCTION

Fig. 9 shows the steady-state and the transient results considering the AFE-VFDs equipped volt-var without dead-band, freq-var with dead-band, and combined freq-volt-var control, considering the functions described in Figs. 2 (a.2), (b.1), and (c), respectively. The active and reactive power at the SG_1, WECS, and AFE-VFDs terminals are shown in Figs. 9 (a), (b), and (c), respectively. Figs. 9 (d) and (e) show the voltage and frequency profiles, respectively. Table 3 summarizes the figures of merit sampled from Fig. 9. In addition, Table 3 presents the figures of merit for AFE-VFDs controlled with PF = 1 ($Q_i^* = 0$) and for the operation of the FPSO electrical power system without AFE-VFDs connection.

From Table 3, with two evaluated steady-states, the FPSO system without AFE-VFDs presents the smallest frequency variations (0.52 Hz and 0.44 Hz), the highest f_{nadir} values (58.64 Hz and 59.11 Hz) and lowest $|RoCoF|$ values. These enhanced frequency parameters are assigned to the inertia contribution when the two 13 MW water injection pump motors are directly coupled to the main busbar. Conversely, without AFE-VFDs, the AVR control represents the only voltage control of the entire power system. The reactive power absorption by the directly coupled motor to the FPSO main busbar deteriorates the voltage-related figure of merit, with voltage variations of 7.05 x 10^{-3} pu and 5.59 x 10^{-3} pu. Reactive power regulation at the AFE-VFD output terminals leads to a voltage regulation improvement compared to the case without AFE-VFD.

From the second line of Table 3, i.e., AFE-VFDs controlled at their terminals with PF = 1, the system inertia decreases, and consequently, frequency-linked parameters show deterioration. The implementation of volt-var control (third line of Table 3), compared to the PF = 1 case, improves voltage variation at the same time that continues to deteriorate frequency parameters. With volt-var implemented, reactive power absorbed for voltage regulation disturbs the frequency. The opposite relation is evidenced when reactive power is injected for frequency regulation (freq-var implemented): the voltage variation is disturbed while frequency parameters show improvement.

During the steady-state intervals, with the incorporation of the volt-var in the freq-var function, i.e. the proposed freq-volt-var, an improvement in voltage variation is observed from 6.58 x 10^{-3} pu (with freq-var) to 4.51 x 10^{-3} pu (with freq-volt-var) - see Table 3. Regarding the transient event caused by the unscheduled interruption of one SG, the voltage sag reaches 0.83 pu and 0.82 pu with freq-var and freq-volt-var strategies, respectively - see Fig. 9 (d). Due to the freq-var and freq-volt-var dead-bands practically not being violated, a similar Δf is obtained for all strategies during steady-state.

Nonetheless, the frequency profile enhancement is noted in the functions with freq-var compared to the volt-var function, as shown in Figs. 9 (f) and (g). For instance, with the SG shutdown at 40 s, the frequency nadir rises from 58.39 Hz (with volt-var) to 58.49 Hz and 58.47 Hz with the employment of freq-var-based strategies (i.e., freq-var, and freq-volt-var, respectively). $|RoCoF|$ value for the disturbance triggered by the shutdown of one wind turbine also shows an improvement: a reduction from 1.87 Hz/s with volt-var to 1.82 Hz/s with combined freq-volt-var for the 70 - 74 s simulated period. Besides, the system inertia constant, calculated using the disturbance triggered by the shutdown of one wind turbine, increases from 2.91 s with volt-var to 2.98 s with freq-volt-var.

V. CONCLUSION

This paper proposed and evaluated the communication-free freq-volt-var function embedded in AFE-VFDs for frequency support in offshore FPSO systems with high WECS penetration. The freq-volt-var prioritized frequency deviations during transient events and voltage deviations during steady-state conditions. This strategy aims to frequency support by processing only reactive power. The evaluation methodology showed that the frequency support via reactive power flow improves the frequency, although it disturbs the FPSO voltage. The incorporation of voltage function to the control guarantees the minimization of these deviations during steady-state and maintains the improvements in frequency at transient events. Steady-state simulation results from the combined freq-volt-var method showed a reduction of 31.5% in voltage variation compared to the freq-var function. The figures of merit for the transient event of SG shutdown, frequency nadir, and inertia constant were enhanced by 0.08 Hz and 2.65%, respectively, compared to the volt-var function.

This means that the improvement in frequency and voltage deviations are achieved with absorption and injection of reactive power by the AFE-VFDs, respectively. This conflicting behavior indicates that it is not possible to improve voltage and frequency deviation simultaneously in FPSO power systems by processing only reactive power. Future work will focus on validating the presented results by means of hardware-in-the-loop simulation validated by experimental data.

APPENDIX

Table 4 shows all FPSO conductors with the cable length and characteristics.

AUTHOR'S CONTRIBUTIONS

MEDEIROS, K.S.: Conceptualization, Data Curation, Formal Analysis, Investigation, Methodology, Software, Validation, Visualization, Writing – Original Draft. **CALLEGARI, J.M. S.**: Conceptualization, Data Curation, Formal Analysis, Investigation, Methodology, Software, Supervision, Validation, Visualization, Writing – Original Draft. **ROCHA, L.F.**: Methodology, Software, Visualization, Writing – Review & Editing. **BRANDAO, D. I.**: Conceptualization, Formal Analysis, Funding Acquisition, Methodology, Project Administration, Resources, Supervision, Visualization, Writing – Review & Editing.

TABLE 4. Conductors characteristics.

Busbar	Tag	R (Ω)	L (mH)	X/R	Length (m)	Cross-sectional area (mm²)	Conductors per phase
Topsides A	l_1	0.0021	0.0115	2.06	95	300	4
	l_2	0.0021	0.0115	2.06	95	300	4
	l_3	0.0022	0.0121	2.07	100	300	4
	l_4	0.0056	0.0197	1.33	40	185	1
	l_5	0.0028	0.0157	2.11	130	300	2
	l_6	0.0057	0.0314	2.08	130	300	2
	l_7	0.0057	0.0314	2.08	130	300	2
	l_8	0.0057	0.0314	2.08	130	300	2
	l_9	0.0070	0.0386	2.08	160	300	2
	l_{10}	0.0330	0.0484	0.55	160	120	1
	l_{11}	0.0104	0.0125	0.45	40	95	1
	l_{12}	0.0330	0.0484	0.55	160	120	1
	l_{13}	0.0268	0.0245	0.34	75	70	1
	l_{14}	0.0672	0.0448	0.25	130	50	1
	l_{15}	0.0268	0.0245	0.34	75	70	1
	l_{16}	0.0672	0.0448	0.25	130	50	1
	l_{17}	0.0517	0.0345	0.25	100	50	1
	l_{18}	0.0672	0.0448	0.25	130	50	1
	l_{19}	0.0775	0.0517	0.25	150	50	1
	l_{20}	0.0672	0.0448	0.25	130	50	1
	l_{21}	0.0143	0.0131	0.35	40	70	1
	l_{22}	0.0517	0.0345	0.25	100	50	1
	l_{23}	0.0672	0.0448	0.25	130	50	1
	l_{24}	0.0672	0.0448	0.25	100	50	1
	l_{25}	0.0207	0.0138	0.25	40	50	1
Topsides B	l_{26}	0.0021	0.0115	2.06	95	300	4
	l_{27}	0.0021	0.0115	2.06	95	300	4
	l_{28}	0.0022	0.0121	2.07	100	300	4
	l_{29}	0.0056	0.0197	1.33	40	185	1
	l_{30}	0.0057	0.0314	2.08	130	300	2
	l_{31}	0.0057	0.0314	2.08	130	300	2
	l_{32}	0.0057	0.0314	2.08	130	300	2
	l_{33}	0.0070	0.0386	2.08	160	300	2
	l_{34}	0.0440	0.0532	0.46	170	95	1
	l_{35}	0.0330	0.0484	0.55	160	120	1
	l_{36}	0.0440	0.0532	0.46	170	95	1
	l_{37}	0.0330	0.0484	0.55	160	120	1
	l_{38}	0.0268	0.0245	0.34	75	70	1
	l_{39}	0.0672	0.0448	0.25	130	50	1
	l_{40}	0.0517	0.0345	0.25	100	50	1
	l_{41}	0.0672	0.0448	0.25	130	50	1
	l_{42}	0.0672	0.0448	0.25	130	50	1
	l_{43}	0.0672	0.0448	0.25	130	50	1
	l_{44}	0.0672	0.0448	0.25	130	50	1
	l_{45}	0.0517	0.0345	0.25	100	50	1
	l_{46}	0.0143	0.0131	0.35	40	70	1
	l_{47}	0.0517	0.0345	0.25	100	50	1
	l_{48}	0.0517	0.0345	0.25	100	50	1
	l_{49}	0.0517	0.0345	0.25	100	50	1
	l_{50}	0.0207	0.0138	0.25	40	50	1
Vessel A	l_{51}	0.0083	0.0459	2.08	95	300	1
	l_{52}	0.0056	0.0197	1.33	100	185	1
	l_{53}	0.0517	0.0345	0.25	100	50	1
	l_{54}	0.0517	0.0345	0.25	100	50	1
	l_{55}	0.0517	0.0345	0.25	100	50	1
	l_{56}	0.0517	0.0345	0.25	100	50	1
	l_{57}	0.0517	0.0345	0.25	100	50	1
	l_{58}	0.0517	0.0345	0.25	100	50	1
Vessel B	l_{59}	0.0083	0.0459	2.08	95	300	1
	l_{60}	0.0056	0.0197	1.33	100	185	1
	l_{61}	0.0517	0.0345	0.25	100	50	1
	l_{62}	0.0517	0.0345	0.25	100	50	1
	l_{63}	0.0517	0.0345	0.25	100	50	1
	l_{64}	0.0517	0.0345	0.25	100	50	1
	l_{65}	0.0517	0.0345	0.25	100	50	1

PLAGIARISM POLICY

This article was submitted to the similarity system provided by Crossref and powered by iThenticate – Similarity Check.

REFERENCES

[1] R. Brown, "FPSO: lessons learned", *IEEE Industry Applications Magazine*, vol. 10, no. 2, pp. 18–23, 2004, doi:10.1109/MIA.2004.1270797.

[2] T.-V. Nguyen, S. de Oliveira Júnior, "Life performance of oil and gas platforms for various production profiles and feed compositions", *Energy*, vol. 161, pp. 583–594, 2018, doi:https://doi.org/10.1016/j.energy.2018.07.121.

[3] Z. Li, H. Zhang, J. Meng, Y. Long, Y. Yan, M. Li, Z. Huang, Y. Liang, "Reducing carbon footprint of deep-sea oil and gas field exploitation by optimization for Floating Production Storage and Offloading", *Applied Energy*, vol. 261, p. 114398, 2020, doi:https://doi.org/10.1016/j.apenergy.2019.114398.

[4] P. Glaum, F. Neumann, T. Brown, "Offshore Wind Integration in the North Sea: The Benefits of an Offshore Grid and Floating Wind", *in 2023 19th International Conference on the European Energy Market (EEM)*, pp. 1–7, 2023, doi:10.1109/EEM58374.2023.10161875.

[5] Q. Yu, Y. Liu, Z. Jiang, L. Li, Y. Zhang, M. Guo, "Study of offshore wind power penetration rate in gas turbine generator platform power grid", *Energy Reports*, vol. 7, pp. 141–146, 2021, doi:https://doi.org/10.1016/j.egyr.2021.02.011, iCPE 2020-The International Conference on Power Engineering.

[6] J. Chu, Y. Lv, Y. Xu, G. Du, D. Sun, P. Yu, "Coordinated Control Strategy for Improving Frequency Stability of Offshore Wind Farms Connected to the Grid through MMC - HVDC Transmission", *in 2022 4th Asia Energy and Electrical Engineering Symposium (AEEES)*, pp. 354–360, 2022, doi:10.1109/AEEES54426.2022.9759790.

[7] R. Blasco-Gimenez, S. Añó-Villalba, J. Rodríguez-D'Derlée, F. Morant, S. Bernal-Perez, "Distributed Voltage and Frequency Control of Offshore Wind Farms Connected With a Diode-Based HVdc Link", *IEEE Transactions on Power Electronics*, vol. 25, no. 12, pp. 3095–3105, 2010, doi:10.1109/TPEL.2010.2086491.

[8] H. Xiao, X. Huang, Y. Huang, Y. Liu, "Self-Synchronizing Control and Frequency Response of Offshore Wind Farms Connected to Diode Rectifier Based HVDC System", *IEEE Transactions on Sustainable Energy*, vol. 13, no. 3, pp. 1681–1692, 2022, doi:10.1109/TSTE.2022.3170717.

[9] K. Wang, Q. Song, B. Zhao, Z. Yu, R. Zeng, "Grid-Forming Control of Offshore Wind Farms Connected With Diode-Based HVdc Links Based on Remote Active Power Regulation", *IEEE Transactions on Sustainable Energy*, vol. 15, no. 2, pp. 1315–1327, 2024, doi:10.1109/TSTE.2023.3343418.

[10] J. Chen, X. Pei, H. Wu, Y. Jin, Z. Zhang, K. Xu, "Steady State Characteristics of Diode Rectifier Unit based Grid-Forming Offshore Wind Power AC System", *in 2022 5th International Conference on Power and Energy Applications (ICPEA)*, pp. 651–656, 2022, doi:10.1109/ICPEA56363.2022.10052224.

[11] M. Mehrabankhomartash, M. Saeedifard, A. Yazdani, "Adjustable Wind Farm Frequency Support Through Multi-Terminal HVDC Grids", *IEEE Transactions on Sustainable Energy*, vol. 12, no. 2, pp. 1461–1472, 2021, doi:10.1109/TSTE.2021.3049762.

[12] A. R. Årdal, T. Undeland, K. Sharifabadi, "Voltage and Frequency Control in Offshore Wind Turbines Connected to Isolated Oil Platform Power Systems", *Energy Procedia*, vol. 24, pp. 229–236, 2012, doi:https://doi.org/10.1016/j.egypro.2012.06.104, selected papers from Deep Sea Offshore Wind R&D Conference, Trondheim, Norway, 19-20 January 2012.

[13] A. R. Årdal, K. Sharifabadi, O. Bergvoll, V. Berge, "Challenges with integration and operation of offshore oil & gas platforms connected to an offshore wind power plant", *in 2014 Petroleum and Chemical Industry Conference Europe*, pp. 1–9, 2014, doi:10.1109/PCICEurope.2014.6900054.

[14] A. A. Adeyemo, E. Tedeschi, "Sizing of Energy Storage for Virtual Inertia Emulation and Primary Frequency Control in Low-Inertia Systems", *in 2022 5th International Conference on Power and Energy Applications (ICPEA)*, pp. 480–486, 2022, doi:10.1109/ICPEA56363.2022.10052579.

[15] C. B. M. Mufalo, B. C. Lima, L. Otremba, R. M. Monaro, M. B. C. Salles, "Sizing of BESS to Support Primary Frequency Control in a O&G FPSO with Wind Power Integration", *in 2023 International Conference on Clean Electrical Power (ICCEP)*, pp. 579–585, 2023, doi:10.1109/ICCEP57914.2023.10247464.

[16] S. Chapaloglou, E. F. Alves, V. Trovato, E. Tedeschi, "Optimal Energy Management in Autonomous Power Systems With Probabilistic Security Constraints and Adaptive Frequency Control", *IEEE Transactions on Power Systems*, vol. 39, no. 1, pp. 1543–1554, 2024, doi:10.1109/TPWRS.2023.3236378.

[17] I. V. Medeiros dos Santos, C. B. Martin Mufalo, L. Otremba, R. M. Monaro, M. B. De Camargo Salles, "Frequency Response Evaluation of an Isolated System Integrating Offshore Wind Generation and an Oil and Gas Platform", *in 2023 15th IEEE International Conference on Industry Applications (INDUSCON)*, pp. 415–421, 2023, doi:10.1109/INDUSCON58041.2023.10374892.

[18] D. d. S. Mota, E. F. Alves, S. D'Arco, S. Sanchez-Acevedo, E. Tedeschi, "Coordination of Frequency Reserves in an Isolated Industrial Grid Equipped With Energy Storage and Dominated by Constant Power Loads", *IEEE Transactions on Power Systems*, vol. 39, no. 2, pp. 3271–3285, 2024, doi:10.1109/TPWRS.2023.3304319.

[19] J. M. S. Callegari, L. A. Vitoi, D. I. Brandao, "VFD-Based Coordinated Multi-Stage Centralized/Decentralized Control to Support Offshore Electrical Power Systems", *IEEE Transactions on Smart Grid*, vol. 14, no. 4, pp. 2863–2873, 2023, doi:10.1109/TSG.2022.3224616.

[20] K. de Sousa Medeiros, L. F. da Rocha, J. M. Soares Callegari, D. I. Brandao, "Frequency-Voltage-var Function for VFD in Oil and Gas Platform with Wind Power", *in 2023 IEEE 8th Southern Power Electronics Conference and 17th Brazilian Power Electronics Conference (SPEC/COBEP)*, pp. 1–8, 2023, doi:10.1109/SPEC56436.2023.10408441.

[21] IEEE1547-2018, "IEEE Standard for Interconnection and Interoperability of Distributed Energy Resources with Associated Electric Power Systems Interfaces", *(Revision of IEEE Std 1547-2003)*, vol. 261, pp. 1–138, 2018.

[22] C.-L. Su, W.-L. Chung, K.-T. Yu, "An Energy-Savings Evaluation Method for Variable-Frequency-Drive Applications on Ship Central Cooling Systems", *IEEE Transactions on Industry Applications*, vol. 50, no. 2, pp. 1286–1294, 2014, doi:10.1109/TIA.2013.2271991.

[23] N. R. Zargari, Z. Cheng, R. Paes, "A Guide to Matching Medium-Voltage Drive Topology to Petrochemical Applications", *IEEE Transactions on Industry Applications*, vol. 54, no. 2, pp. 1912–1920, 2018, doi:10.1109/TIA.2017.2785759.

[24] W. Liu, T. Tarasiuk, C.-L. Su, M. Gorniak, M. Savaghebi, J. C. Vasquez, J. M. Guerrero, "An Evaluation Method for Voltage Dips in a Shipboard Microgrid Under Quasi-Balanced and Unbalanced Voltage Conditions", *IEEE Transactions on Industrial Electronics*, vol. 66, no. 10, pp. 7683–7693, 2019, doi:10.1109/TIE.2018.2885722.

[25] Z. Yang, J. Sun, Y. Tang, M. Huang, X. Zha, "An Integrated Dual Voltage Loop Control for Capacitance Reduction in CHB-Based Regenerative Motor Drive Systems", *IEEE Transactions on Industrial Electronics*, vol. 66, no. 5, pp. 3369–3379, 2019, doi:10.1109/TIE.2018.2854606.

[26] H. M. A. Antunes, D. I. Brandao, V. H. M. Biajo, M. H. S. Alves, F. S. Oliveira, S. M. Silva, "Floating, Production, Storage, and Offloading Unit: A Case Study Using Variable Frequency Drives", *IEEE Transactions on Industry Applications*, vol. 59, no. 4, pp. 4764–4772, 2023, doi:10.1109/TIA.2023.3258420.

[27] J. M. Guerrero, M. Chandorkar, T.-L. Lee, P. C. Loh, "Advanced Control Architectures for Intelligent Microgrids—Part I: Decentralized and Hierarchical Control", *IEEE Transactions on Industrial Electronics*, vol. 60, no. 4, pp. 1254–1262, 2013, doi:10.1109/TIE.2012.2194969.

[28] IEC, "Mobile and fixed offshore units - Electrical installations - Part 1: General requirements and conditions", *IEC 61892-1:2019*, 2019.

[29] N. A. E. R. Corporation, "Fast Frequency Response Concepts and Bulk Power System Reliability Need: NERC Inverter-Based Resource Performance Task Force", *Fast Frequency Response*, pp. 1–29, 2020.

[30] T. Inoue, H. Taniguchi, Y. Ikeguchi, K. Yoshida, "Estimation of power system inertia constant and capacity of spinning-reserve support generators using measured frequency transients", *IEEE Transactions on Power Systems*, vol. 12, no. 1, pp. 136–143, 1997, doi:10.1109/59.574933.

BIOGRAPHIES

Kassiane de S. Medeiros received the B.Sc. degree in electrical engineering, in 2012, and the M.Sc. degree in electrical engineering, in 2015, both from the Pontifical Catholic University of Minas Gerais, Belo Horizonte, Brazil. She is currently working toward the Ph.D. degree in electrical engineering with the Federal University of Minas Gerais, Belo Horizonte, Brazil. Her current research and technical interests include offshore energy, power-quality issues, and control strategies from power electronic converters.

João Marcus S. Callegari received the B.Sc. degree in electrical engineering from the Federal University of Viçosa, Brazil, in 2019, the M.Sc. degree in electrical engineering from the Federal Center of Technological Education of Minas Gerais, Brazil, in 2021, and the doctorate degree in electrical engineering at the Federal University of Minas Gerais, Brazil, in 2024. His current research and technical interests include the design and control of grid-connected multifunctional inverters, the reliability of power electronics-based systems, and AC microgrids. Mr. Callegari was the recipient of the President Bernardes Silver Medal in 2019 and the IEEE IAS CMD Student Thesis Contest 2022 (Non-PhD Category).

Lorrana F. da Rocha received the B.Sc. degree in automation and control engineering from the Federal Center for Technological Education of Minas Gerais, Brazil, in 2018. She received the M.Sc. degree in electrical engineering from the Federal University of Juiz de Fora, Brazil, in 2020. She is currently working toward the Ph.D. degree with the Norwegian University of Science and Technology working on design of power electronics architecture and control methods for a high-voltage direct current power train for offshore wind. She also has a background in coordinated control of offshore systems and integration of offshore wind energy. Her research interests include power electronic converters, modeling and control strategies, and power train drive systems. In addition to the issues of lowering prices and boosting efficiency of offshore wind farms.

Danilo I. Brandao received the doctorate degree in electrical engineering from the State University of Campinas (Unicamp), Brazil, in 2015. He was visiting positions at Colorado School of Mines (2009 and 2013), Università degli Studi di Padova (2014) and Norwegian University of Science and Technology (2018 and 2020). He is currently an assistant professor at Federal University of Minas Gerais (UFMG), Brazil. His main research interests are control of grid-tied converters and microgrids. He is a member of SOBRAEP.